Glutathione-Depleting Organic Metal Adjuvants for Effective NIR-II Photothermal Immunotherapy

Yun Chen[1,2], Peiying He[1], Deblin Jana[2], Dongdong Wang[2], Menghao Wang[3], Peiyuan Yu[3], Wei Zhu[1]*, Yanli Zhao[2]*

Dr. Y. Chen, P. He, Prof. W. Zhu

MOE International Joint Research Laboratory on Synthetic Biology and Medicines, School of Biology and Biological Engineering, South China University of Technology, Guangzhou 510006, P. R. China.

Dr. Y. Chen, Dr. D. Jana, Dr. D. Wang, Prof. Y. Zhao

Division of Chemistry and Biological Chemistry, School of Physical and Mathematical Sciences, Nanyang Technological University, 21 Nanyang Link, 637371, Singapore.

M. Wang, P. Yu

Shenzhen Grubbs Institute and Department of Chemistry, Guangdong Provincial Key Laboratory of Catalysis, Southern University of Science and Technology, Shenzhen, 518055, P. R. China.

*E-mail: zhuwei86@scut.edu.cn; zhaoyanli@ntu.edu.sg

ABSTRACT. Although photothermal immunotherapy (PTI) is a compelling strategy for tumor therapy, the development of promising photothermal agents to overcome the insufficient immunogenicity of tumor cells and the poor immune response encountered in PTI is still challenging. Herein, we present commercial small-molecule-based organic metal adjuvants (OMAs) with second near-infrared photoacoustic and photothermal properties as well as the ability to perturb redox homeostasis to potentiate immunogenicity and immune responsiveness. OMAs,

assembled from charge-transfer complexes and characterized by a broad substrate scope, high accessibility, and flexibly tuned optical properties, demonstrate strong phototherapeutic and adjuvant abilities via the depletion of glutathione and cysteine, and subsequently elicit systemic immunity by evoking immunogenic cell death, promoting dendritic cell maturation, and increasing T cell infiltration. Furthermore, programmed cell death protein 1 antibody can be employed to synergize with OMAs to suppress tumor immune evasion and ultimately improve the treatment outcomes. This study unlocks new paradigms to provide a versatile OMA-based scaffold for future practical applications.

Keywords: cancer treatment, glutathione depletion, organic metal adjuvants, photoacoustic imaging, photothermal immunotherapy

1. Introduction

Photothermal immunotherapy (PTI), an emerging cancer therapy method that integrates photothermal therapy (PTT) with immunotherapy, can directly cause tumor cell death in an immunogenic manner and work synergistically with immunotherapy to potentiate the immune response.[1] The therapeutic efficiency of PTI is often modest, owing to the inadequate immunogenicity of tumor cells and poor immune response.[2] PTT triggers immunogenic cell death (ICD) by releasing damage-associated molecular patterns (DAMPs) to induce dendritic cell (DC) maturation and increase T cell infiltration, thereby initiating the antitumor immune responses.[3] Evidence from recent studies has validated the pivotal role of reactive oxygen species (ROS) production and endoplasmic reticulum stress for the exposure of DAMPs.[3b, 4] Therefore, the development of photothermal agents (PTAs) with effective ROS production capacities provides a promising direction for improving the immunogenicity of tumor cells.[5] The antioxidant system, mainly consisting of glutathione (GSH), can reduce ROS levels and lead to immunosuppression

and attenuation of antitumor efficacy.[6] Therefore, it is imperative to exploit GSH-consuming PTAs to leverage the ICD effect of PTT and to serve as adjuvants to elevate immune responsiveness.

Second near-infrared (NIR-II) (1000–1350 nm) PTAs, based on a variety of inorganic and organic materials, have recently attracted considerable attention owing to their advantages of deep tissue penetration, high maximum permission energy, and good sensitivity and signal-noise ratio.[7] So far, NIR-II PTAs have been explored in combination with immunoadjuvant therapy, genome editing-based therapy, or immune checkpoint blockade therapy to achieve effective PTI.[8] Among them, inorganic NIR-II PTAs, consisting of non-metallic materials, noble metals, and transition metal materials, exhibit good photothermal effects as well as tunable and controllable morphologies, but suffer from potential leakage and weak biodegradability.[9] Organic NIR-II PTAs, containing small-molecule photosensitizers,[10] semiconducting polymers,[11] and organic radicals,[12] exhibit low side-effects and good biocompatibility,[7] but sophisticated design and complex production requirements often hinder their applications.[10b, 13] An organic metal is an organic material that possesses the electrical, magnetic, and optical properties of a metal while retaining the degradability, biocompatibility, adjustability, and processability associated with an organic material. There are two categories of organic metals: polymeric hydrocarbons (polyacetylene, polyaniline, and polypyrrole) and charge-transfer complexes (CTCs).[14] Among them, CTCs arising from the interactions between electron donors and electron acceptors have attracted increasing attention in organic light-emitting diodes,[15] organic photovoltaic devices, [16] and other biological fields[17] owing to their flexible photophysical/physicochemical properties. To date, only a few CTCs with NIR-II absorption, including the co-assembly of 3,3',5,5'-tetramethylbenzidine (TMB) and tetracyanoquinodimethane (TCNQ), have been reported to realize ROS-mediated ferroptosis,[18] utilization of perylene-TCNQ nanoparticles for NIR-II photothermal antibacterial applications,[19] and use of TMB and its dication structure (TMB^{++}) for

NIR-II photoacoustic (PA) imaging.[20] However, exploiting organic metals with intracellular response ability for their applications in PTI has not yet been reported.

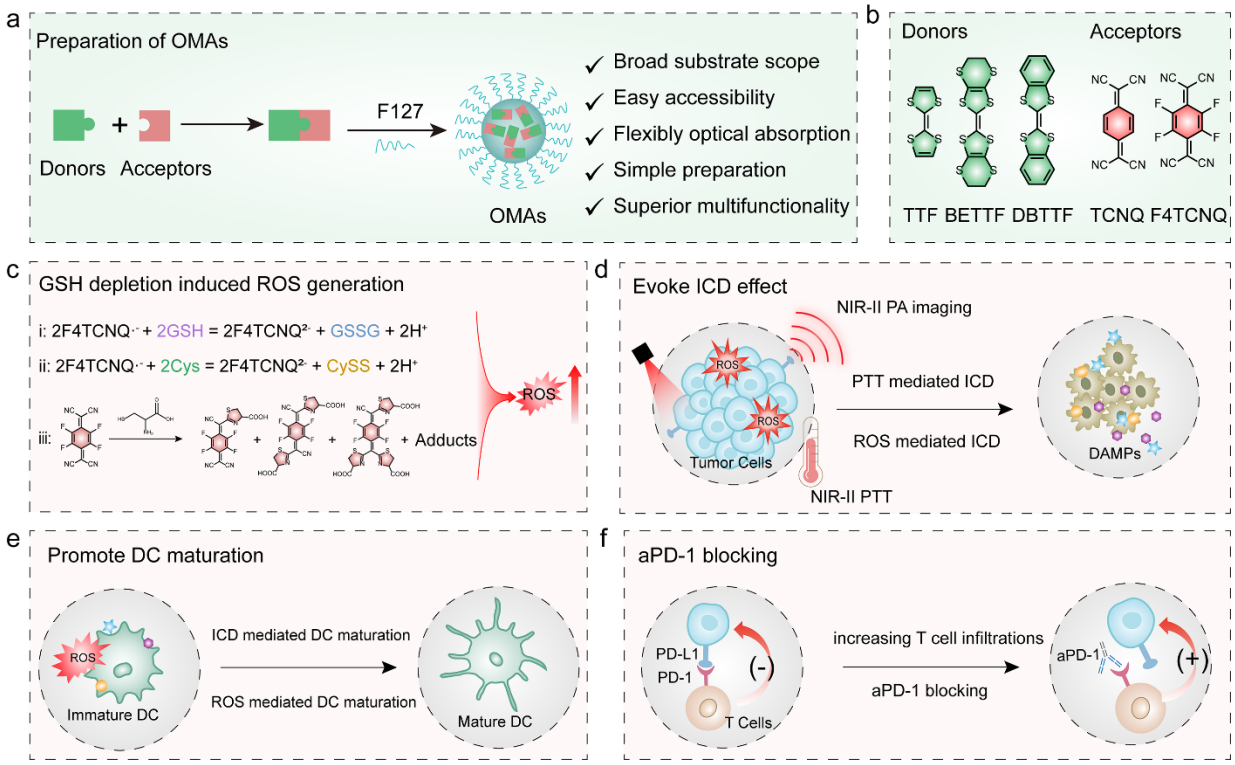

Figure 1. Scheme of organic metal adjuvant (OMA)-mediated second near-infrared (NIR-II) photothermal immunotherapy (PTI). a) Preparation of OMAs. b) Chemical structures of donors and acceptors. c) Reaction mechanism of OMAs with glutathione (GSH) and cysteine (Cys). d) Mechanism of immunogenic cell death (ICD) induction. e) Mechanism of dendritic cell (DC) maturation. f) Mechanism of programmed cell death protein 1 antibody (aPD-1) blockade.

Herein, we report a convenient strategy to engineer small-molecule-based organic metal adjuvants (OMAs) with NIR-II phototheranostic and adjuvant abilities to facilitate effective PTI (Figure 1). OMAs constructed via the supramolecular assembly of commercially available donors and acceptors can achieve good NIR-II photothermal performance and PA imaging ability by optimizing the constituting components. The formed OMAs demonstrate the ability to oxidize GSH

and cysteine (Cys). OMAs react with Cys via a cycloaddition reaction to block the intracellular biosynthesis of GSH, which can directly disrupt intracellular redox homeostasis and boost ROS accumulation. Synergistic GSH depletion and NIR-II PTT not only potentiate immunogenicity by evoking abundant ICD, but also enhance the immune response by promoting DC maturation and increasing T cell infiltration. With the assistance of the programmed cell death protein 1 antibody (aPD-1), GSH-depleting NIR-II PTI can erase the primary tumors and significantly delay distant tumor growth. As a result, this strategy provides a superior platform for strengthening the therapeutic effect of PTI, which can aid in the development of an OMA pool to meet the increasing requirements of tumor treatment.

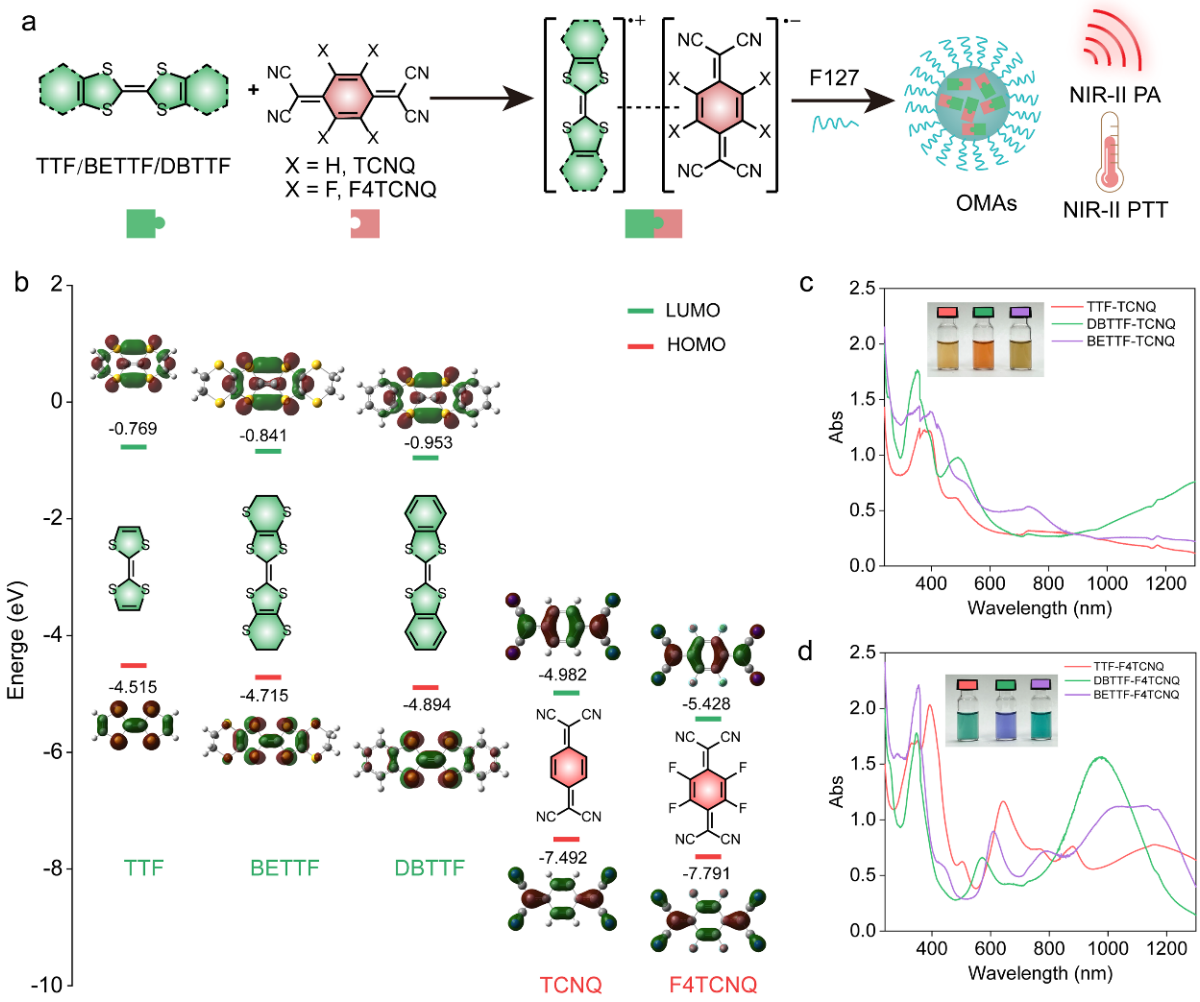

Figure 2. Characterization of OMAs. a) Preparation process of OMAs. b) Energy levels of tetrathiofulvalinium (TTF), bis(ethylenedithio)tetrathiafulvalene (BETTF), dibenzotetrathiafulvalene (DBTTF), 7,7,8,8-tetracyanoquinodimethane (TCNQ), and 2,3,5,6-tetrafluoro-7,7,8,8-tetracyanoquinodimethane (F4TCNQ). c) Ultraviolet (UV)/visible (Vis)-NIR absorption spectra of TTF-TCNQ, DBTTF-TCNQ, and BETTF-TCNQ. d) UV/Vis-NIR absorption spectra of TTF-F4TCNQ, DBTTF-F4TCNQ, and BETTF-F4TCNQ.

2. Results and Discussion

2.1. Preparation of OMAs. OMAs are easily constructed via supramolecular assembly of commercially available small-molecule donors and acceptors. The structures of substrates and the degree of charge-transfer (CT) significantly affect the optical absorption properties of organic metals.[15] As a proof of concept, tetrathiofulvalinium (TTF)- 7,7,8,8-tetracyanoquinodimethane (TCNQ) system, the first discovered organic metal in 1973,[21] was applied to realize NIR-II PTI by variating the molecular structures or formula of the substrates. Three common commercially available donors, TTF and its derivatives (dibenzo tetrathiafulvalene (BDTTF) and bis(ethylenedithio)tetrathiafulvalene (BETTF)) and two acceptors (TCNQ and 2,3,5,6-tetrafluoro-7,7,8,8-tetracyanoquinodimethane (F4TCNQ)) were used to prepare OMAs using the reprecipitation method. Poly(ethylene glycol)-block-poly(propylene glycol)-block-poly(ethylene glycol) (F127) was used to improve the water dispersibility (Figure 2a). Their combinations formed six different types of OMAs: TTF-TCNQ, DBTTF-TCNQ, BETTF-TCNQ, TTF-F4TCNQ, DBTTF-F4TCNQ, and BETTF-F4TCNQ. According to the calculated energy levels, the highest occupied molecular orbitals (HOMOs) of the donors (–4.515, –4.715, and –4.894 eV) were higher than the lowest unoccupied molecular orbitals (LUMOs) of the acceptors (–4.982 and –5.428 eV) (Figure 2b), suggesting that the formation of ground-state charge transfer complexes (GSCs) and

CT could spontaneously occur in the six OMAs.[15] Note that the energy gaps (ΔE_g, the difference between the HOMO of the donor and LUMO of the acceptor) of the F4TCNQ-based OMAs are larger than those of the TCNQ-based OMAs, indicating stronger driving forces of CT in the F4TCNQ-based system.[18] Afterwards, related absorption spectra were obtained to further corroborate the successful formation of CTCs. As seen in Figure 2c and d, OMAs formed by F4TCNQ showed significant NIR-II absorption with peaks at 976, 1081, and 1161 nm, whereas the TCNQ-based OMAs did not exhibit obvious absorption in this region. The red-shift of spectra to the NIR-II region agrees with the calculated ΔE_g of TTF-F4TCNQ (0.913 eV), BETTF-F4TCNQ (0.713 eV), and DBTTF-F4TCNQ (0.534 eV). Notably, both the donor and acceptor molecules in the tetrahydrofuran (THF) solution presented no obvious absorption in the NIR-II region (Figure S1, Supporting Information). Therefore, OMAs are believed to be superior systems for tumor therapy because of their broad substrate scope, ease of preparation, high accessibility, and flexibly-tuned optical properties.

2.2. Characterization of TTF-F4TCNQ. Although the mass extinction coefficients of DBTTF-F4TCNQ (25.1 L g^{-1} cm^{-1}) and BETTF-F4TCNQ (21.1 L g^{-1} cm^{-1}) were higher than that of TTF-F4TCNQ (17.7 L g^{-1} cm^{-1}) at 1064 nm, the stabilities of DBTTF-F4TCNQ and BETTF-F4TCNQ were unsatisfactory due to the high hydrophobicity of DBTTF and BETTF. Obvious precipitation occurred in the DBTTF-F4TCNQ and BETTF-F4TCNQ solutions after only one day of storage (Figure S2). Surprisingly, TTF-F4TCNQ exhibited long-term stability, as the hydrodynamic size remained stable for seven days (Figure S3a). Moreover, TTF-F4TCNQ presented good stability with a negligible size change when dispersed in phosphate-buffered saline (PBS), Dulbecco's modified Eagle's medium (DMEM), or Roswell Park Memorial Institute (RPMI-1640) solution (Figure S3b). Considering its simplicity, representativeness, stability, and good NIR-II absorption

properties, TTF-F4TCNQ was selected for subsequent experiments. As shown in Figure 3a, TTF-F4TCNQ showed a uniform size distribution of 25.8 nm, which was consistent with the transmission electron microscopy (TEM) results. For the interesting NIR-II absorption property, TTF-F4TCNQ was used for photothermal research. As shown in Figure S4, TTF-F4TCNQ exhibited excellent photothermal effect with a photothermal conversion efficiency of up to 47.0%, as compared to the negligible temperature rise of individual TTF nanoparticles and F4TCNQ nanoparticles under identical conditions (Figure 3b). The photothermal behavior of TTF-F4TCNQ was concentration- and laser-density-dependent under 1064 nm irradiation (Figures S5 and S6). Furthermore, TTF-F4TCNQ exhibited a high photothermal stability after four cycles of heating and natural cooling (Figure 3c).

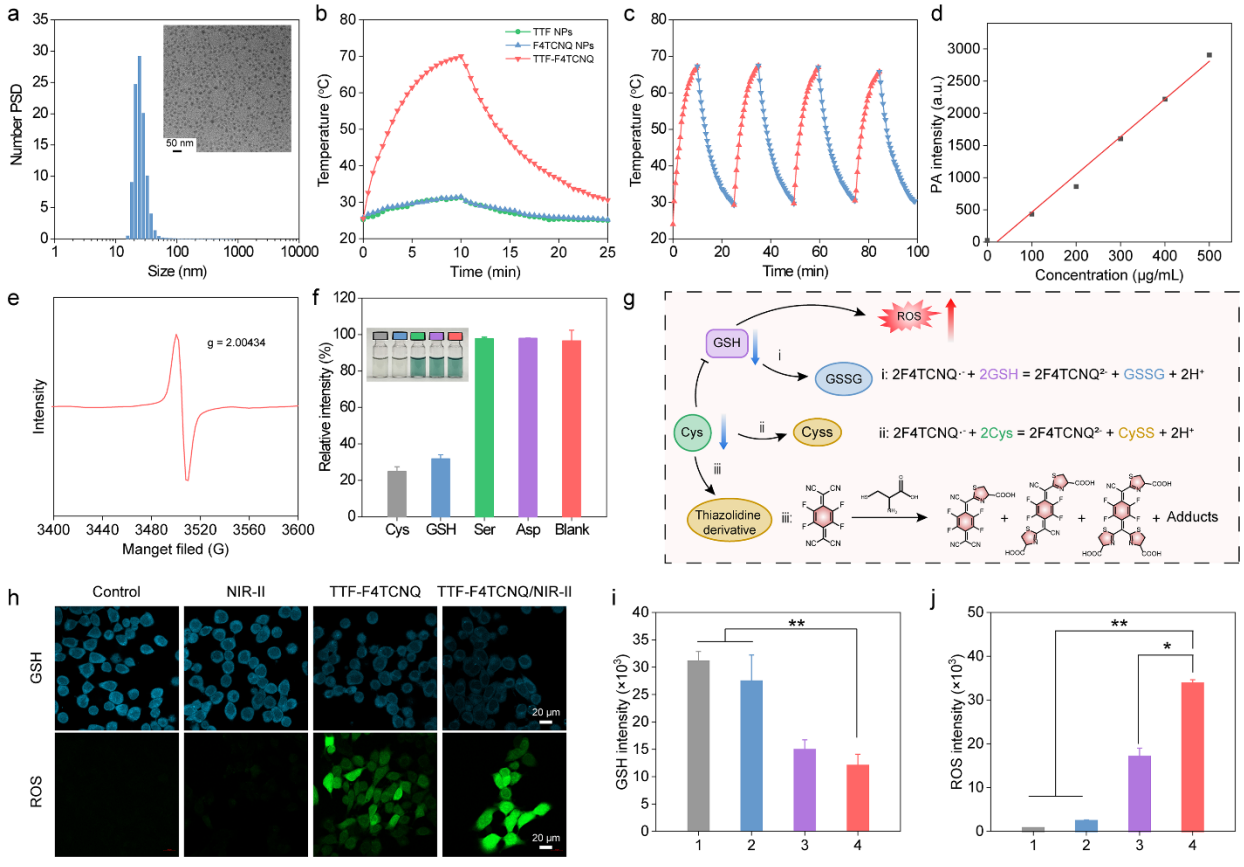

Figure 3. Properties of TTF-F4TCNQ. a) Dynamic light scattering (DLS) and transmission electron microscopy (TEM) characterization of TTF-F4TCNQ. b) Photothermal heating curves of TTF nanoparticles (TTF NPs), F4TCNQ nanoparticles (F4TCNQ NPs), and TTF-F4TCNQ responding to 1064 nm laser irradiation (1 W cm^{-2}). c) Temperature variation of TTF-F4TCNQ with repeated 1064 nm irradiation (1 W cm^{-2}) on/off for four cycles. d) Photoacoustic (PA) signals of TTF-F4TCNQ under 1064 nm laser. e) Electron spin resonance (ESR) spectrum of TTF-F4TCNQ. f) Absorption spectra of TTF-F4TCNQ with the addition of Cys, GSH, L-serine (Ser), and L-aspartic acid (Asp), respectively (n = 3). g) Schematic illustration of GSH depletion-induced reactive oxygen species (ROS) generation. h) Confocal laser scanning microscopy (CLSM) images and i) mean fluorescence intensities (MFIs) of GSH levels after virous treatments (n = 3). h) CLSM images and j) MFIs of ROS levels after virous treatments (n = 3). Treatments: 1. PBS; 2. NIR-II; 3. TTF-F4TCNQ; 4. TTF-F4TCNQ/NIR-II. Data were shown as mean ± standard deviation (SD). Statistical significance was calculated via one-way analysis of variance (ANOVA) with a Tukey post-hoc test. $^{*}p < 0.05$ and $^{**}p < 0.01$.

Notably, the heat induced by PTAs after irradiation can cause the expansion of surrounding tissue to generate ultrasound signals, which can be utilized for PA imaging.[22] Specifically, PA imaging in the NIR-II region holds great promise because of the small amount of light scattering and deep-tissue penetration. However, the exploitation of organic NIR-II PA agents is still limited because of the complex synthetic routes to build conjugated systems to reach this region.[23] Owing to its good photothermal effect, the NIR-II PA performance of TTF-F4TCNQ was further explored. As shown in Figure 3d and Figure S7, TTF-F4TCNQ emitted bright PA signals at 1064 nm, and the intensity was linearly enhanced with elevated concentrations, suggesting that TTF-F4TCNQ could be a promising contrast agent for NIR-II PA imaging.

Apart from theoretical calculations (Figure 2b), the existence of CT was further confirmed by electron spin resonance (ESR) measurements. As indicated in Figure 3e, the ESR of TTF-F4TCNQ displayed a strong signal at 3505.4 Gauss (the corresponding g factor is 2.0038), indicating the existence of unpaired electrons.[24] Because of quinoid–diradicaloid interconversion, F4TCNQ also showed biradical characteristics, while TTF showed no obvious ESR signal (Figure S8). Due to the presence of unpaired electrons, TTF-F4TCNQ can undergo oxidation reactions with reductive substances.[4a, 25] GSH is the main intracellular antioxidant that plays a major role in the detoxification of intracellular ROS.[6a, 26] Cys is an essential amino acid for the biosynthesis of GSH, and the depletion of Cys can directly inhibit GSH biosynthesis.[27] GSH and Cys were separately added to TTF-F4TCNQ solution, and the reaction was monitored using an ultraviolet (UV)/visible (Vis)-NIR spectrophotometer. The absorbance of TTF-F4TCNQ gradually decreased and the color of the solution faded after incubation with GSH and Cys, while the addition of the representative control amino acids, L-serine (Ser) and L-aspartic acid (Asp), caused only minor changes in the absorption spectrum (Figure 3f and Figure S9). To gain deep insights into the reaction mechanism, F4TCNQ was reacted with GSH and Cys, and mass spectrometry (MS) was used to identify the products in the reaction system. As shown in Figure 3g and Figures S10-S13, MS spectra showed the generation of glutathione disulfide (GSSG) from GSH and cystine (CySS) from Cys in the presence of F4TCNQ. MS also revealed the product of a thiazolidine derivative in the Cys system, indicating that F4TCNQ could react with the 1,2-aminothiol group of Cys, as reported in the literature.[28] Therefore, TTF-F4TCNQ can block GSH generation and promote GSH consumption to invalidate its antioxidant effects.

The GSH-exhausting strategy mitigates intracellular ROS consumption to directly disrupt intracellular redox homeostasis for boosting the ROS accumulation, which is different from the mechanism of chemodynamic therapy-induced ROS generation.[29] Moreover, the depletion of

GSH not only promotes ICD induction of tumor cells, but also shows the potential to promote DC maturation and attenuate immunosuppression.[6a] A fluorescence thiol probe was used to evaluate whether TTF-F4TCNQ could downregulate intracellular GSH levels. As indicated in Figure 3h, strong fluorescence was observed in the confocal laser scanning microscopy (CLSM) images of untreated 4T1 breast cancer cells, whereas the addition of TTF-F4TCNQ drastically reduced the fluorescence intensity by approximately 52.1% (Figure 3i). Similar results were obtained via the quantitative analysis of the cell lysate using Ellman's assay, which indicated that the GSH levels decreased upon increasing the concentration of TTF-F4TCNQ (Figure S14). Due to the dynamic balance between intracellular GSH and ROS levels, the intracellular ROS levels of 4T1 cells were monitored using 2',7'-dichlorofluorescin diacetate (DCFH-DA) as the probe. The green fluorescence intensity of TTF-F4TCNQ-treated group significantly increased by 20.1-folds relative to that of the untreated group (Figure 3h, j). Intriguingly, under NIR-II light irradiation, GSH depletion and ROS generation were 1.2-folds and 2.0-folds higher than those in the unirradiated group. Low GSH and high ROS levels can be attributed to the elevated temperature under NIR-II irradiation[8c]. As shown in Figure S15 of the Supporting Information, the consumption of GSH and Cys was improved with an increase in temperature. Notably, only NIR-II irradiation exerted no obvious effects on GSH depletion and ROS generation.

2.3. In vitro photothermal ablation and TTF-F4TCNQ-mediated PTI. To evaluate the biocompatibility and potential cytotoxicity of TTF-F4TCNQ, human embryonic kidney (HEK 293) and 4T1 cells were incubated with TTF-F4TCNQ. TTF-F4TCNQ exhibited a dose-dependent cancer cell inhibition effect with a median inhibitory concentration (IC_{50}) of ~61.8 μg mL^{-1} due to GSH consumption and ROS accumulation (Figure 4a). Importantly, TTF-F4TCNQ had negligible

toxicity towards HEK 293 cells, probably because normal cells exhibit stronger antioxidant capacities and lower GSH levels than cancer cells.[30]

Owing to its excellent photothermal properties, the cytotoxicity of TTF-F4TCNQ against 4T1 cells with NIR-II irradiation was further investigated. As shown in Figure 4b, TTF-F4TCNQ caused significant cell death compared to the control group after NIR-II irradiation. For instance, treatment with 40 μg mL^{-1} of TTF-F4TCNQ only caused ~ 23.9% cell death, whereas over 87.3% of tumor cells were killed after NIR-II irradiation. A live/dead cell staining assay confirmed the remarkable phototherapeutic efficacy of TTF-F4TCNQ (Figure S16). Furthermore, the cell apoptosis study of TTF-F4TCNQ with or without NIR-II irradiation was determined by annexin V-fluorescein isothiocyanate/propidium iodide staining. The apoptosis rate (early and advanced apoptosis) of TTF-F4TCNQ treated cells was 27.0% owing to the depletion of GSH, whereas 63.4% cell apoptosis was observed after NIR-II irradiation, confirming the high photothermal effect of TTF-F4TCNQ (Figure S17). In contrast, no appreciable cell death was observed upon treatment with NIR-II light alone.

To test the synergistic effect of GSH depletion with NIR-II PTT of TTF-F4TCNQ, three key ICD markers, calreticulin (CRT), high mobility group box 1 (HMGB-1) and adenosine triphosphate (ATP), were detected. As shown in Figure 4c, CLSM images showed no obvious CRT signals in the control and NIR-II groups. The treatment of TTF-F4TCNQ mediated a moderate CRT translocation to the surface of cell membrane, while its combination with NIR-II irradiation (TTF-F4TCNQ/NIR-II) induced the significant expression of CRT on the cell surface. In addition, HMGB-1 was located predominantly in the nuclei of 4T1 cells and gradually released from the nuclei after TTF-F4TCNQ treatment. In the TTF-F4TCNQ/NIR-II group, almost all HMGB-1 was released from the nucleus (Figure 4c). Moreover, 4T1 cells treated with TTF-F4TCNQ/NIR-II

showed 1.3- and 1.9-folds higher ATP secretion than those treated with the TTF-F4TCNQ and control groups, respectively (Figure 4d).

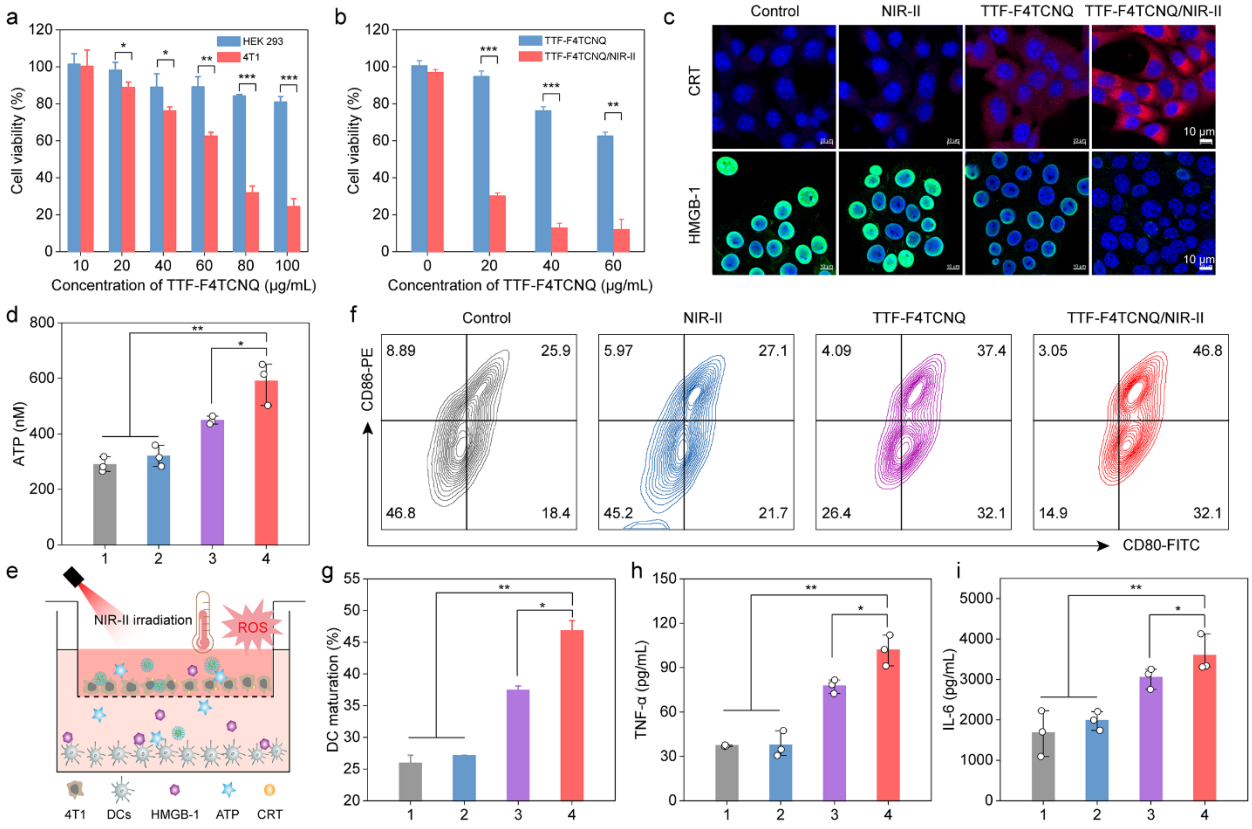

Figure 4. In vitro TTF-F4TCNQ-mediated PTI. a) Cell viabilities of HEK 293 and 4T1 cells after incubation with TTF-F4TCNQ at different concentrations (n = 5). b) Cell viabilities of 4T1 cells after incubation with TTF-F4TCNQ with or without NIR-II light irradiation for 5 min (1 W cm^{-2}) (n = 5). c) CLSM images showing calreticulin (CRT) exposure and high mobility group box 1 (HMGB-1) release in 4T1 tumor cells following various treatments (n = 3). d) Adenosine triphosphate (ATP) secretion from 4T1 cells following various treatments (n = 3). e) Schematic illustration of the Transwell system. f) Flow cytometry assay and g) quantitative analysis of DC maturation (gated on $CD11c^+$ DCs) induced by different treatments (n = 3). h) tumor necrosis factor (TNF)-α and i) interleukin (IL)-6 content in DC suspensions from (f) (n = 3). Treatments: 1. PBS; 2. NIR-II; 3. TTF-F4TCNQ; 4. TTF-F4TCNQ/NIR-II. Data were shown as mean ± SD. Statistical

significance was calculated via ANOVA with a Tukey post-hoc test. $^{*}p < 0.05$, $^{**}p < 0.01$, and $^{***}p < 0.001$.

DCs, one of the most important antigen-presenting cells (APCs), can be activated to initiate the innate and adaptive immunity.[31] To verify whether GSH depletion could enhance the immune response by promoting DC maturation, intracellular ROS levels in bone marrow-derived dendritic cells (BMDCs) were determined after incubation with TTF-F4TCNQ. The green fluorescence was significantly enhanced after incubation with TTF-F4TCNQ compared to that observed in the untreated cells (Figure S18). The frequency of mature DCs ($CD11c^{+}CD80^{+}CD86^{+}$, the hallmark of DC maturation) was measured using flow cytometry. Interestingly, intracellular ROS generation in the TTF-F4TCNQ treatment group directly promoted DC maturation to approximately 48.8% versus 36.2% of the control group (Figure S19).

For ICD-inducted DC maturation, a Transwell system was utilized, in which the upper chambers were seeded with 4T1 tumor cells, while the lower chambers were simultaneously grown with BMDCs (Figure 4e). Photoirradiated TTF-F4TCNQ significantly increased the maturation of DCs (46.6%), which was 1.3-folds or 1.8-folds higher than those of TTF-F4TCNQ (36.2%) and the control group (25.6%), respectively (Figure 4f, g). Moreover, tumor necrosis factor (TNF)-α and interleukin 6 (IL-6), two cytokines related to DC activation, were monitored using enzyme-linked immunosorbent assay (ELISA) kits. Both TNF-α and IL-6 showed the highest expression levels in TTF-F4TCNQ/NIR-II group, indicating that DAMPs secreted from dying cancer cells can effectively trigger DC maturation (Figure 4h, i). Collectively, CRT exposure, HMGB-1 release, ATP secretion, DC maturation, and cytokine secretion verified the synergistic action of GSH depletion and NIR-II PTT function of TTF-F4TCNQ/NIR-II for immune activation.

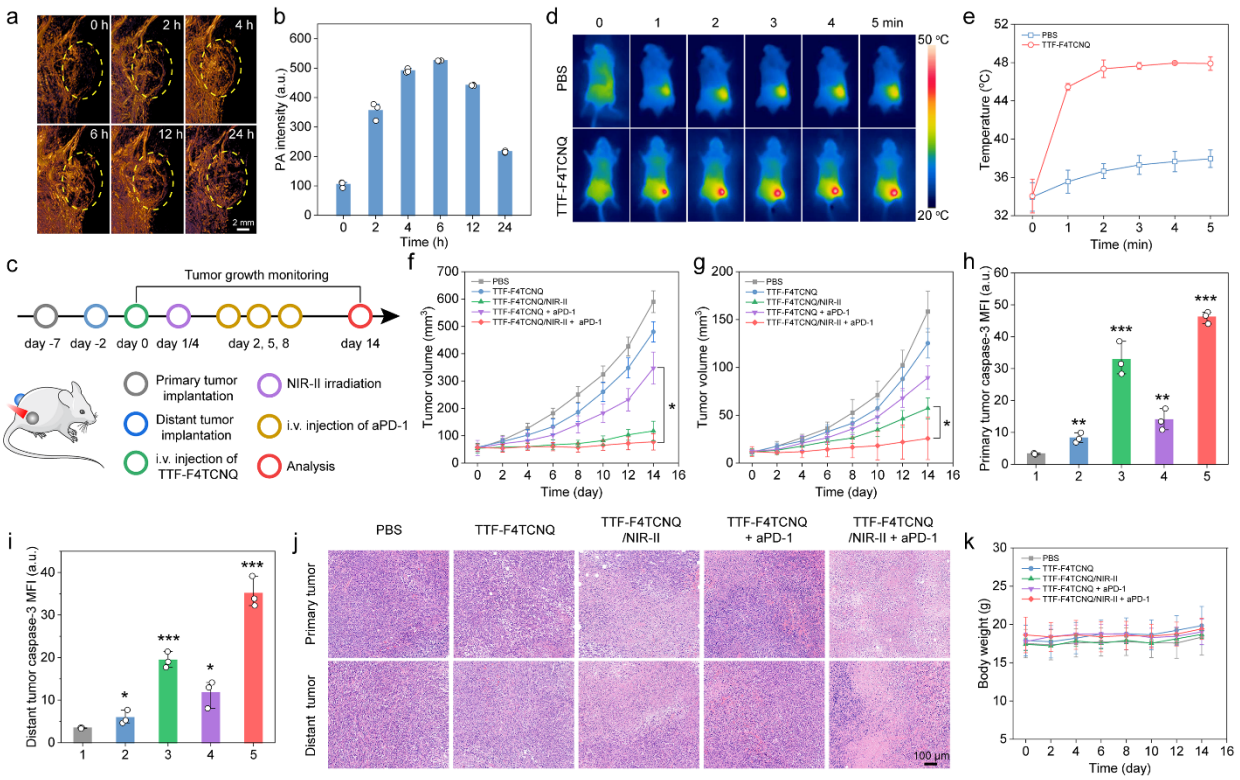

Figure 5. In vivo PA imaging and antitumor performance of TTF-F4TCNQ. a) In vivo PA imaging of the 4T1-bearing tumor site after intravenous injection of TTF-F4TCNQ (1064 nm, n = 3). b) Relative PA intensity of corresponding PA images in (a) (n = 3). c) Treatment schedule for in vivo antitumor study. d) Infrared thermal images of the mice injected with PBS or TTF-F4TCNQ in response to 1064 nm irradiation (1 W cm^{-2}, 5 min) (n = 3). e) Temperature of the mice tumors following different treatments (n = 5). Growth curves for f) primary tumors and g) distant tumors following different treatments (n = 5). Quantitative analysis of caspase-3 levels in h) primary and i) distant tumors after different treatments (n = 3). j) Hematoxylin and eosin (H&E) staining of the primary and distant tumor tissues. k) Body weight changes of the mice under different treatments. Treatments: 1. PBS; 2. TTF-F4TCNQ; 3. TTF-F4TCNQ/NIR-II; 4. TTF-F4TCNQ + aPD-1; 5. TTF-F4TCNQ/NIR-II + aPD-1. Data were shown as mean ± SD. The statistical significance in (f) and (g) was measured by a two-tailed Student's t-test. The statistical significance in (h) and (i) was calculated via ANOVA with a Tukey post-hoc test. $^{*}p < 0.05$, $^{**}p < 0.01$, and $^{***}p < 0.001$.

2.4. In vivo PA imaging and anti-tumor performance of TTF-F4TCNQ-mediated PTI. To visualize the accumulation of TTF-F4TCNQ in the tumor regions, NIR-II PA imaging was performed. PA signals in the tumor sites gradually enhanced and peaked at 6 h after intravenous administration of TTF-F4TCNQ (Figure 5a, b), indicating that TTF-F4TCNQ had strong PA performance with enhanced permeability and retention in the tumor.

To evaluate the antitumor activity of TTF-F4TCNQ-mediated NIR-II PTI, a bilateral 4T1 tumor-bearing BALB/c mouse model was established. The right-side tumor was used as the primary tumor for GSH depletion therapy and NIR-II PTT, and the left-side tumor was designed as the distant tumor to investigate the immunological antitumor effect. To enhance the antitumor effect of TTF-F4TCNQ, aPD-1, which can counter the "escape" of cancer cells from immunity, was selected in combination with TTF-F4TCNQ for tumor therapeutics.[3a] Mice were randomized into five groups: (1) PBS, (2) TTF-F4TCNQ, (3) TTF-F4TCNQ/NIR-II, (4) TTF-F4TCNQ + aPD-1, and (5) TTF-F4TCNQ/NIR-II + aPD-1. Under the guidance of PA imaging, the primary tumors were irradiated with NIR-II light after 6 h the intravenous administration of TTF-F4TCNQ. Subsequently, aPD-1 was administered to the mice every three days for 3 cycles (Figure 5c). As seen from Figure 5d, e, upon NIR-II irradiation, the temperature of tumors in the TTF-F4TCNQ group increased from 34.0 °C to 47.9 °C in 5 min to realize mild-temperature PTT and potentiate immunological responses.[32] However, the temperature of tumors in PBS group only increased to approximately 38.0 °C.

The growth of primary and distant tumors in the different groups was monitored every two days. After treatment, the TTF-F4TCNQ group exhibited slight tumor inhibition, with the tumor inhibitory rate (TIR) of the primary tumor was 20.5% and the distant tumor was 18.9%.

Encouragingly, excellent antitumor efficiency was observed in the TTF-F4TCNQ/NIR-II group, where the TIR of the primary tumors was 80.1% and the TIR of the abscopal tumors reached 63.9% (Figure 5f, g). Moreover, with the assistance of aPD-1, the TTF-F4TCNQ/NIR-II group delayed 86.8% of primary tumor growth and 83.8% of distant tumor growth. Immunofluorescence staining revealed that TTF-F4TCNQ-mediated PTI caused high cell apoptosis in primary and distant tumors, as reflected by the red fluorescence signals of the CY3-labeled anticaspase-3 antibody (Figure 5h, i and Figure S20). In particular, the MFIs of TTF-F4TCNQ/NIR-II group were 4.0- and 10.0-folds higher than those of TTF-F4TCNQ or PBS in primary tumors, and 3.3- and 5.7-folds higher than those in distant tumors, respectively. In addition, the MFIs of TTF-F4TCNQ/NIR-II + aPD-1 group further increased 1.4- and 1.8-folds relative to those in the TTF-F4TCNQ/NIR-II group. Hematoxylin and eosin (H&E) staining showed the similar outcome that the most obvious tumor tissue shrinkage and damage was found in the primary and distant tumors of TTF-F4TCNQ/NIR-II and TTF-F4TCNQ/NIR-II + aPD-1 treated mice (Figure 5j). These results demonstrated that TTF-F4TCNQ-mediated PTI could eradicate primary tumors and significantly inhibit distant tumor growth, and its combination with PD-1 antibody could further increase the therapeutic outcome.

During treatment, no noticeable change in body weight was found among the groups (Figure 5k). Furthermore, histological analysis of the major organs (heart, liver, spleen, lung, and kidney) in TTF-F4TCNQ/NIR-II and TTF-F4TCNQ/NIR-II + aPD-1 groups did not reveal organ damage or obvious pathological changes (Figure S21), indicating that TTF-F4TCNQ had high biosafety and good biocompatibility.

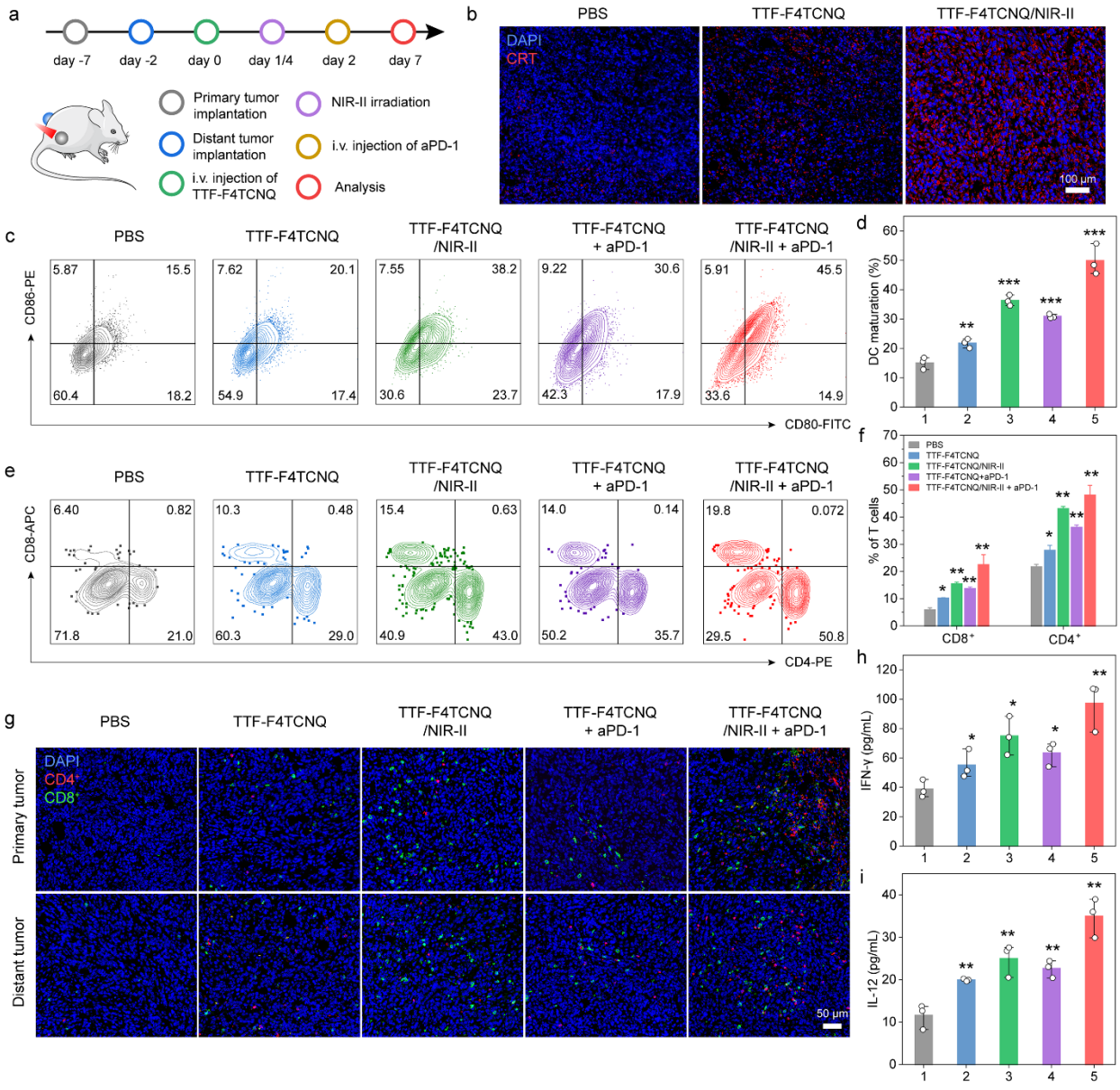

Figure 6. In vivo NIR-II PTI. a) Schedule for tumor model implantation and TTF-F4TCNQ-mediated PTI. b) Immunofluorescence staining showing CRT in the primary tumor tissues (n = 3). c) Flow cytometric examination and d) quantification of mature DCs in spleen after different treatments (n = 3). e) Flow cytometric assay and f) relative populations of T lymphocytes ($CD8^+$ and $CD4^+$) in spleen after different treatments (n = 3). g) Immunofluorescence staining of $CD4^+$ (red) and $CD8^+$ (green) in the primary and distant tumor tissues after various treatments (n = 3). Enzyme-linked immunosorbent assay (ELISA) analysis of cytokines, h) IL-12 and i) interferon

(IFN)-γ (n = 3). Treatments: 1. PBS; 2. TTF-F4TCNQ; 3. TTF-F4TCNQ/NIR-II; 4. TTF-F4TCNQ + aPD-1; 5. TTF-F4TCNQ/NIR-II + aPD-1. Data were shown as mean ± SD. The statistical significance was calculated via ANOVA with a Tukey post-hoc test. $^{*}p < 0.05$, $^{**}p < 0.01$, and $^{***}p < 0.001$.

2.5. Immune response activation after NIR-II PTI. As TTF-F4TCNQ shows strong antitumor efficiency, we evaluated its capacity to induce immunotherapy under irradiation by analyzing various immunological processes, including ICD induction, DC maturation, T cell infiltration, and cytokine release. ICD induction was verified by immunofluorescence staining of CRT and HMGB-1 markers in the primary tumor sections, which showed that photo-irradiated TTF-F4TCNQ significantly amplified CRT expression and HMGB-1 release (Figure 6a, b and Figure S22). For instance, the MFIs of CY3-labeled anti-CRT antibody in the primary tumor of the photo-irradiated TTF-F4TCNQ group were significantly increased by 6.3- and 3.2-folds relative to those of the PBS and TTF-F4TCNQ groups, respectively (Figure 6b and Figure S23). Furthermore, TTF-F4TCNQ treatment moderately facilitated DC maturation in the spleen, from 15.2% to 21.8% compared to that in the PBS group. The population of mature DCs in TTF-F4TCNQ group further increased to 36.3% after NIR-II irradiation. Photo-irradiated TTF-F4TCNQ with aPD-1 blockade exhibited the highest level of DC maturation (49.9%), which was 2.3-, 1.4- and 1.6-folds higher than that of TTF-F4TCNQ, TTF-F4TCNQ/NIR-II, and TTF-F4TCNQ + aPD-1 groups, respectively (Figure 6c, d). Similar results for DC maturation were also observed in tumor-draining lymph nodes (Figure S24).

Mature DCs play an important role in antigen presentation to T lymphocytes, thus promoting intratumoral infiltration of cytotoxic T lymphocytes (CTLs, $CD8^+$ T cells). The photo-irradiated TTF-F4TCNQ group induced 17.5% and 12.9% of $CD8^+$ CTL activation in the primary and distant

tumors, respectively (Figures S25 and S26), which were 1.9- and 1.8-folds higher than that of TTF-F4TCNQ group. With the help of aPD-1, the frequency of $CD8^+$ CTLs further increased to 25.6% and 15.7% in the primary and distant tumors, respectively. Consistently, the content of $CD8^+$ CTLs in the spleen was also the most significantly elevated in the TTF-F4TCNQ/NIR-II + aPD-1 group (Figure 6e, f). In addition to CTL recruitment, TTF-F4TCNQ/NIR-II + aPD-1 group also prompted the most significant activation of $CD4^+$ T helper cells (Figure 6e, f), showing 1.1-, 1.7-, and 2.2-fold increases in population compared to the TTF-F4TCNQ/NIR-II, TTF-F4TCNQ, and PBS groups. Moreover, the enhanced tumor infiltration of $CD8^+$ and $CD4^+$ T cells in the TTF-F4TCNQ/NIR-II + aPD-1 group were verified by immunofluorescence staining of tumor sections (Figure 6g). Interleukin 12 (IL-12) and interferon γ (IFN-γ) cytokines in serum were analyzed using ELISA kits after different treatments (Figure 6h, i). Consistent with the DC maturation results, photoirradiated TTF-F4TCNQ with the assistance of aPD-1 triggered the highest cytokine secretion. For instance, the IFN-γ level induced by TTF-F4TCNQ/NIR-II + aPD-1 (97.1 pg mL^{-1}) was 1.3- and 1.8-folds higher than that of TTF-F4TCNQ/NIR-II group (74.9 pg mL^{-1}) or TTF-F4TCNQ group (55.1 pg mL^{-1}). Collectively, these results indicated that TTF-F4TCNQ/NIR-II + aPD-1 treatment could activate a robust immune response and the proposed pathway of the GSH-depleting OMAs for effective NIR-II photothermal immunotherapy was listed in Figure S27.

3. Conclusion

The development of promising organic NIR-II PTAs to realize effective PTI is highly desirable.[1b] Organic metals combine the merits of inorganic and organic materials to fabricate NIR-II PTAs, owing to their flexibly-tuned optical properties, broad substrate scope, and easy accessibility.[33] Here, we reported OMAs with high immunogenicity and adjuvanticity to achieve effective NIR-II PA imaging-guided PTI. By varying the constituent components, the absorption

of OMAs could be conveniently adjusted to NIR-II absorption (Figure 2c, d). In particular, OMAs formed by TTF-F4TCNQ demonstrated strong NIR-II absorption ability and exerted excellent photothermal effects (Figure 3b, c). ROS play a vital role in cancer immunotherapy, as they not only elevate the immunogenicity of tumor cells, but also serve as adjuvants to APCs for the immune response.[34] Here, TTF-F4TCNQ could directly convert GSH to GSSG, as well as Cys to CySS. In addition, F4TCNQ with cyano unit could react with the 1,2-aminothiol group of Cys, which would further block GSH generation, as Cys is an essential amino acid for the biosynthesis of GSH (Figure 3e–g and Figures S7–S11). The consumption of GSH together with NIR-II PTT treatment can directly disrupt intracellular redox homeostasis to boost ROS accumulation and promote ICD induction, DC maturation, T cell infiltration, and cytokine secretion, which cam further induce a systemic immune response and exhibit superior antitumor efficiency. With the assistance of aPD-1 in suppressing tumor immune evasion, OMAs can further enhance the immune response and achieve a much better therapeutic effect.

In summary, we developed GSH-depleting NIR-II PTAs based on OMAs with high immunogenicity and adjuvant properties. Upon integration with aPD-1, the combined system achieved effective PA imaging-guided PTI of primary and distant tumors. Owing to their flexibly-tuned optical properties, broad substrate scope, easy accessibility, simple preparation, and superior multifunctionality, OMAs not only show highly efficient therapeutic effects, but also represent a novel solution to meet the challenging requirements of tumor treatment. Therefore, the findings of this work can aid in the development of advanced PTI systems and their clinical translation.

4. Experimental Section

Instrumentation. UV/Vis-NIR absorption spectra were collected on a UV-3600 spectrometer (Shimadzu, Japan). The particle sizes were recorded using a Nano ZS ZEN3600 DLS analyzer

(Malvern, UK). TEM images were collected using a JEM 2100plus microscope (JEOL, Japan). CLSM images were acquired using a LSM 800 microscope (ZEISS, Germany). Flow cytometry analysis was performed using a Fortessa X20 (BD Biosciences, America). PA signal was measured using LOIS-3D (TomoWave Laboratories, USA). All animal experiments were performed according to the animal guidelines of the Nanyang Technological University Institutional Animal Care and Use Committee (NTU-IACUC), with protocol number A19016.

Chemicals. Unless otherwise noted, all reagents were obtained from Sigma-Aldrich. CRT antibody (Catalog No. MA1-91034, dilution 1:100) was purchased from Thermo Fisher Scientific. HMGB-1 antibody was purchased from Abcam. Caspase-3 antibody was purchased from Servicebio (GB11532, dilution 1:500). Alexa Fluor 700 anti-mouse CD45, APC anti-mouse CD8a, APC anti-mouse CD11c, aPD-1, FITC anti-mouse CD3, FITC anti-mouse CD80, PE anti-mouse CD4, and PE anti-mouse CD86 antibodies and ELISA kits (TNF-α, IL-6, IL-12, and IFN-γ) were purchased from BioLegend. The secondary antibody (CY3-goat anti-rabbit IgG) was purchased from Servicebio (GB21303; dilution, 1:300). Deionized (DI) water was used for all aqueous experiments.

Preparation of OMAs. The donor (40 mM in THF solution, 100 μL), acceptor (40 mM in dimethyl sulfoxide (DMSO) solution, 100 μL), and F127 (8 mM in THF solution, 100 μL) were mixed, and the solution was injected into DI water (4.0 mL) under vigorous stirring to obtain the OMAs. Finally, the prepared nanoparticles were dialyzed against DI water using a 10 kDa cut-off membrane to remove impurities.

Stability test. TTF-F4TCNQ (100 μL, 1 mg mL^{-1}) was mixed with 900 μL of PBS buffer, DMEM, and RPMI-1640 solution. After incubation for 12 h, DLS measurements were taken to study the stability. For long-term stability, TTF-F4TCNQ (1 mL, 100 μg mL^{-1}) was subjected to DLS measurements on days 0, 3, 5, and 7.

Computational setup. Density functional theory calculations were performed to study the molecular orbitals of these compounds. All calculations were performed using Gaussian 16 code. The Def2SVP basis set and ωb97xd functionals were used.[35] Charges and multiplicities of these compounds were set to 0 and 1, respectively.

Photothermal effect. The TTF-F4TCNQ solution in water (1.0 mL; 0, 20, 40, 60, 80, and 100 μg mL^{-1}) was irradiated using a 1064 nm laser. For the power density-dependent photothermal property, TTF-F4TCNQ aqueous solution (1.0 mL, 100 μg mL^{-1}) with various power densities was irradiated by a 1064 nm laser, and the variation in temperature was recorded by a thermal camera. To investigate photostability, TTF-F4TCNQ (1.0 mL, 100 μg mL^{-1}) was first irradiated by a 1064 nm laser for 10 min and then cooled for 15 min. The experiment was conducted for four cycles. Photothermal conversion efficiency (η) was calculated as follows:

$$\eta = \frac{\frac{m_D c_D}{\tau_s}(T_{Max} - T_{Surr}) - Q_{Dis}}{I(1 - 10^{-A})}$$

where T_{Max} is the maximum steady-state temperature, T_{Surr} is the ambient temperature of the environment, τ_s is the sample-system time constant, m_D and c_D are the mass and heat capacity (4.2 J/g) of deionized (DI) water, respectively, Q_{Dis} expresses the heat associated with NIR-II light absorption by the solvent (DI water), I is the laser power, and A is the absorbance of the TTF-F4TCNQ aqueous solution at 1064 nm.

GSH depletion assay. TTF-F4TCNQ (500 μL, 400 μg mL^{-1}), amino acid (40 μL, 0.01 mol L^{-1}), and DI water (1460 μL) were mixed in the vial, and then the mixture was incubated at 37 °C for 24 h. Then the absorption spectra were measured at different time intervals. To investigate the effect of temperature on GSH and Cys depletion, TTF-F4TCNQ (500 μL, 400 μg mL^{-1}), GSH or Cys (40 μL, 0.01 mol L^{-1}), and DI water (1460 μL) were mixed in the vial, and the mixture was

incubated at 25, 37, 42, and 47 °C for 5 min. Then, the absorption spectra were measured using a UV/Vis-NIR spectrometer.

Intracellular GSH assay. 4T1 cells were treated with TTF-F4TCNQ (20, 40, and 60 μg mL^{-1}) with or without 1064 nm irradiation (1 W cm^{-2}, 5 min). After another 12 h of incubation, GSH level was determined using a GSH/GSSG assay kit. Likewise, the GSH content was also detected by the addition of the fluorescence thiol dye (Thiol Tracker Violet), and then subjected to observation under a CLSM.

Intracellular ROS assay. DCFH-DA was used as the fluorescent probe to measure the ROS levels. 4T1 cells were treated with TTF-F4TCNQ (40 μg mL^{-1}) with or without 1064 nm irradiation (1 W cm^{-2}, 5 min). After 12 h of incubation, cells were stained with DCFH-DA and incubated for another 30 min. After washed with PBS twice, the cells were subjected to CLSM observation.

In vitro cytotoxicity assays. 4T1 or HEK 293 cells were seeded onto a 96-well plate at a density of 7000 cells/well. TTF-F4TCNQ at different known concentrations was then added to the cell medium. After 24 h of incubation, 10 μL of 3-(4,5-cimethylthiazol-2-yl)-2,5-diphenyl tetrazolium bromide (MTT) working solution was added. After incubation for 2 h, the cell medium was replaced with a DMSO solution (150 μL). The absorbance of the plate was recorded at 490 nm wavelength. As for the toxicity of TTF-F4TCNQ after NIR-II irradiation, 4T1 cells were first treated with TTF-F4TCNQ (20, 40, and 60 μg mL^{-1}) and then applied to 1064 nm irradiation (1 W cm^{-2}, 5 min). The cells were then cultured for 24 h and subjected to a standard MTT assay. HEK 293 cells were cultured to investigate the biosafety of TTF-F4TCNQ using the same procedure.

ICD detection. For the immunofluorescence detection of CRT expression levels, 4T1 cells were incubated with TTF-F4TCNQ (40 μg mL^{-1}) with or without 1064 nm light (1 W cm^{-2}, 5 min). After cultured for 6 h, the cells were fixed with 4% paraformaldehyde (PFA) for 15 min, permeabilized with 0.1% PBST for 30 min. After blocking with 3% fetal bovine serum (FBS), the cells were then

treated with the anti-CRT antibody at 4 °C overnight. After incubation, Alexa Fluor 568 conjugated secondary antibody was applied to for 2 h. Afterwards, the cells were stained with Hoechst 33342 for 15 min and subjected to CLSM analysis.

For immunofluorescence detection of HMGB-1 release, 4T1 cells were incubated with TTF-F4TCNQ (40 μg mL^{-1}) with or without 1064 nm light (1 W cm^{-2}, 5 min). After cultured for 6 h, the cells were washed twice with PBS, fixed with 4% PFA for 15 min, permeabilized with 0.1% PBST for 30 min. After blocking with 3% FBS, the cells were then treated with the anti-HMGB-1 antibody at 4 °C overnight. After incubation, Alexa Fluor 488-conjugated secondary antibody was applied for 2 h. Afterwards, the cells were stained with Hoechst 33342 for 15 min and subjected to CLSM analysis.

For ATP detection, the supernatants of 4T1 cells after various treatments were collected and centrifuged (1500 rpm, 5 min). The ATP concentration was quantified using an ATP assay kit.

In vitro DC activation. BMDCs were freshly collected from BALB/c mice (purchased from InVivos Pte Ltd, Singapore), according to a well-established DC maturation protocol.[36] BMDCs were first treated with TTF-F4TCNQ (40 μg mL^{-1}) for 6 h and then treated with anti-CD11c-APC, anti-CD80-FITC, and anti-CD86-PE antibodies for 20 min. Afterwards, the cells were then subjected to flow cytometry analysis.

A 12-well Transwell system was used for ICD-induced DC maturation. Briefly, 4T1 cells were seeded in the upper wells and allowed to adhere overnight, followed by treatment with TTF-F4TCNQ (40 μg/mL) with or without 1064 nm irradiation (1 W cm^{-2}, 5 min). Subsequently, the upper wells were transferred and co-incubated with the BMDCs in the bottom wells. After cultured for 6 h, the supernatants were collected for cytokine detection. DCs were harvested and treated

with the anti-CD11c-APC, anti-CD80-FITC, and anti-CD86-PE antibodies for 20 min and then subjected to flow cytometry analysis.

PA imaging of TTF-F4TCNQ in vitro and in vivo. TTF-F4TCNQ aqueous solutions (0, 100, 200, 300, 400, and 500 μg mL^{-1}) were injected into different PA glass tubes, and the PA tubes were then placed in the LOIS-3D machine to measure the PA intensity. For in vivo PA imaging, TTF-F4TCNQ aqueous solution (5.0 mg kg^{-1}) was intravenously injected into 4T1 tumor-bearing mice. PA imaging of mice before TTF-F4TCNQ injection was used as the control.

In vivo anti-tumor efficacy. Mice received subcutaneous injection of 4T1 cells at both the right (5×10^6 cells) and left flanks (1×10^7 cells), which were termed as primary and distant tumors, respectively. When the primary tumors reached ~50 mm^3, the mice were randomized into five groups (n = 5): (1) PBS, (2) TTF-F4TCNQ, (3) TTF-F4TCNQ/NIR-II, (4) TTF-F4TCNQ + aPD-1, and (5) TTF-F4TCNQ/NIR-II + aPD-1. For mice in groups (2), (3), (4) and (5), TTF-F4TCNQ (5.0 mg kg^{-1}) was intravenously injected. Six hours post-injection, the primary tumors in groups (3) and (5) were applied with 1064 nm irradiation (1 W cm^{-2}, 5 min), and the changes in temperature were detected using a thermal camera. On days 2, 5, and 8 post-injection, aPD-1 was intravenously injected (1.0 mg kg^{-1}) in groups (4) and (5). Tumor volume was calculated as follows: tumor volume (V) = (tumor length) × $(\text{tumor width})^2/2$. All mice were sacrificed on day 14 post injection. Primary and distant tumors were collected for caspase 3 staining and histological analysis.

Immunofluorescence of CRT and HMGB-1. Mice received subcutaneous injection of 4T1 cells at both the right (5×10^6 cells) and left flanks (1×10^7 cells), which were termed as primary and distant tumors, respectively. When the primary tumors reached ~50 mm^3, TTF-F4TCNQ was intravenously injected into the mice (5.0 mg kg^{-1}). Six hours post-injection, the right-side tumors were applied to 1064 nm irradiation for 5 min. On day 2, aPD-1 (1.0 mg kg^{-1}) was intravenously injected into the mice. On day 7 post-injection, the blood, tumor-draining lymph nodes, tumors,

and spleens of mice were harvested. Primary tumors were harvested for CRT and HMGB-1 immunofluorescence analysis.

DC maturation and T cell infiltration in tumors. Single-cell suspension solutions of tumors and spleens were collected via digestion with collagenase I and IV (1.0 mg/mL) and DNase I (0.2 mg/mL) at 37 °C for 2 h. To investigate T cell infiltration in tumors, single-cell suspensions of tumors were added with anti-CD45-AF700, anti-CD3-FITC, anti-CD4-PE, and anti-CD8-APC antibodies for 20 min and then subjected to flow cytometry analysis. To study the maturation of DCs, single-cell suspensions of tumor-draining lymph nodes and spleens were treated with anti-CD11c-APC, anti-CD80-FITC, and anti-CD86-PE antibodies and then subjected to flow cytometry analysis. The serum levels of IL-12 and IFN-γ were measured using ELISA kits.

Statistical analysis. All data are calculated as the mean ± SD. Statistical significances were analyzed by ANOVA with a Tukey post-hoc test and unpaired two-tailed Students' *t*-test using GraphPad Prism software. For the statistical analysis, $^{*}p < 0.05$, $^{**}p < 0.01$, and $^{***}p < 0.001$ were considered to be statistically significant.

Acknowledgements. This work was supported by the National Natural Science Foundation of China (21972047), Guangdong Provincial Pearl River Talents Program (2019QN01Y314), Program for Guangdong Introducing Innovative and Entrepreneurial Teams (2019ZT08Y318), Natural Science Foundation of Guangdong Province China (2021A1515010724), China Postdoctoral Science Foundation (2021M691063), Fundamental Research Funds for the Central Universities of China, Singapore Agency for Science, Technology and Research (A*STAR) AME IRG grant (A20E5c0081), and Singapore National Research Foundation Investigatorship (NRF-NRFI2018-03). Computational work was supported by Center for Computational Science and Engineering at Southern University of Science and Technology.

Author contributions

Y.Z., W.Z., and Y.C. conceived the study concept and designed the study. Y.C., P.H., D.J., and D.W. conducted the experiments. M.W. and P.Y. performed theoretical calculations. Y.Z., W.Z., and Y.C. contributed to the interpretation of results and writing of this manuscript.

Supporting Information

Supporting Information is available from the Wiley Online Library or from the author.

References

[1] a) X. Li, J. F. Lovell, J. Yoon, X. Chen, *Nat. Rev. Clin. Oncol.* **2020**, *17*, 657; b) M. Chang, Z. Hou, M. Wang, C. Li, J. Lin, *Adv. Mater.* **2021**, *33*, 2004788.

[2] M. Wang, M. Chang, C. Li, Q. Chen, Z. Hou, B. Xing, J. Lin, *Adv. Mater.* **2021**, *34*, 2106010.

[3] a) D. S. Chen, I. Mellman, *Immunity* **2013**, *39*, 1; b) D. V. Krysko, A. D. Garg, A. Kaczmarek, O. Krysko, P. Agostinis, P. Vandenabeele, *Nat. Rev. Cancer* **2012**, *12*, 860.

[4] a) Z. Zhou, K. Ni, H. Deng, X. Chen, *Adv. Drug. Deliv. Rev.* **2020**, *158*, 73; b) W. Li, J. Yang, L. Luo, M. Jiang, B. Qin, H. Yin, C. Zhu, X. Yuan, J. Zhang, Z. Luo, Y. Du, Q. Li, Y. Lou, Y. Qiu, J. You, *Nat. Commun.* **2019**, *10*, 3349.

[5] A. D. Garg, A. M. Dudek, G. B. Ferreira, T. Verfaillie, P. Vandenabeele, D. V. Krysko, C. Mathieu, P. Agostinis, *Autophagy* **2013**, *9*, 1292.

[6] a) Z. Zhou, H. Wu, R. Yang, A. Xu, Q. Zhang, J. Dong, C. Qian, M. Sun, *Sci. Adv.* **2020**, *6*, eabc4373; b) M. Zhang, Z. Dai, S. Theivendran, Z. Gu, L. Zhao, H. Song, Y. Yang, C. Yu, *Nano Today* **2021**, *36*, 101035.

[7] C. Xu, K. Pu, *Chem. Soc. Rev.* **2021**, *50*, 1111.

[8] a) X. Chen, Y. Chen, H. Xin, T. Wan, Y. Ping, *Proc. Natl. Acad. Sci. USA* **2020**, *117*, 2395; b) H. Tang, X. Xu, Y. Chen, H. Xin, T. Wan, B. Li, H. Pan, D. Li, Y. Ping, *Adv. Mater.* **2021**, *33*, 2006003; c) M. Wen, J. Ouyang, C. Wei, H. Li, W. Chen, Y. N. Liu, *Angew. Chem. Int. Ed.* **2019**, *58*, 17425.

[9] Z. Yu, W. K. Chan, Y. Zhang, T. T. Y. Tan, *Biomaterials* **2021**, *269*, 120459.

[10] a) X. Deng, Z. Shao, Y. Zhao, *Adv. Sci.* **2021**, *8*, 2002504; b) H. S. Jung, P. Verwilst, A. Sharma, J. Shin, J. L. Sessler, J. S. Kim, *Chem. Soc. Rev.* **2018**, *47*, 2280.

[11] C. Zhang, Z. Zeng, D. Cui, S. He, Y. Jiang, J. Li, J. Huang, K. Pu, *Nat. Commun.* **2021**, *12*, 2934.

[12] B. Tang, W. L. Li, Y. Chang, B. Yuan, Y. Wu, M. T. Zhang, J. F. Xu, J. Li, X. Zhang, *Angew. Chem. Int. Ed.* **2019**, *58*, 15526.

[13] H. Xiang, L. Zhao, L. Yu, H. Chen, C. Wei, Y. Chen, Y. Zhao, *Nat. Commun.* **2021**, *12*, 218.

[14] M. R. Bryce, L. C. Murphy, *Nature* **1984**, *309*, 119.

[15] D. Shen, W. Chen, M. Lo, C. S. Lee, *Mater. Today Energy* **2021**, *20*, 100644.

[16] K. Vandewal, K. Tvingstedt, A. Gadisa, O. Inganas, J. V. Manca, *Nat. Mater.* **2009**, *8*, 904.

[17] Y. Wang, W. Zhu, W. Du, X. Liu, X. Zhang, H. Dong, W. Hu, *Angew. Chem. Int. Ed.* **2018**, *57*, 3963.

[18] C. Ou, W. Na, W. Ge, H. Huang, F. Gao, L. Zhong, Y. Zhao, X. Dong, *Angew. Chem. Int. Ed.* **2021**, *60*, 8157.

[19] S. Tian, H. Bai, S. Li, Y. Xiao, X. Cui, X. Li, J. Tan, Z. Huang, D. Shen, W. Liu, P. Wang, B. Z. Tang, C. S. Lee, *Angew. Chem. Int. Ed.* **2021**, *60*, 11758.

[20] Z. Wang, P. K. Upputuri, X. Zhen, R. Zhang, Y. Jiang, X. Ai, Z. Zhang, M. Hu, Z. Meng, Y. Lu, Y. Zheng, K. Pu, M. Pramanik, B. Xing, *Nano Res.* **2018**, *12*, 49.

[21] J. Ferraris, D. O. Cowan, V. Walatka, J. H. Perlstein, *J. Am. Chem. Soc.* **1973**, *95*, 948.

[22] Y. Wu, F. Zeng, Y. Zhao, S. Wu, *Chem. Soc. Rev.* **2021**, *50*, 7924.

[23] Y. Jiang, P. K. Upputuri, C. Xie, Z. Zeng, A. Sharma, X. Zhen, J. Li, J. Huang, M. Pramanik, K. Pu, *Adv. Mater.* **2019**, *31*, 1808166.

[24] H. Xiang, Q. Yang, Y. Gao, D. Zhu, S. Pan, T. Xu, Y. Chen, *Adv. Funct. Mater.* **2020**, *30*, 1909938.

[25] a) X. Wang, W. Wang, M. Peng, X. Zhang, *Biomaterials* **2021**, *266*, 120474; b) B. Yuan, C. Xu, R. Zhang, D. Lv, S. Li, D. Zhang, L. Liu, C. Fernandez, *Biosens. Bioelectron.* **2017**, *96*, 1.

[26] Y. Xiong, C. Xiao, Z. Li, X. Yang, *Chem. Soc. Rev.* **2021**, *50*, 6013.

[27] L. Y. Niu, Y. Z. Chen, H. R. Zheng, L. Z. Wu, C. H. Tung, Q. Z. Yang, *Chem. Soc. Rev.* **2015**, *44*, 6143.

[28] a) G. Liang, H. Ren, J. Rao, *Nat. Chem.* **2010**, *2*, 54; b) Z. Zheng, P. Chen, M. Xie, C. Wu, Y. Luo, W. Wang, J. Jiang, G. Liang, *J. Am. Chem. Soc.* **2016**, *138*, 11128.

[29] Z. Tang, Y. Liu, M. He, W. Bu, *Angew. Chem. Int. Ed.* **2019**, *58*, 946.

[30] Y. Liu, W. Zhen, Y. Wang, S. Song, H. Zhang, *J. Am. Chem. Soc.* **2020**, *142*, 21751.

[31] a) V. Trujillo-Alonso, E. C. Pratt, H. Zong, A. Lara-Martinez, C. Kaittanis, M. O. Rabie, V. Longo, M. W. Becker, G. J. Roboz, J. Grimm, M. L. Guzman, *Nat. Nanotechnol.* **2019**, *14*, 616; b) H. Liang, X. Wu, G. Zhao, K. Feng, K. Ni, X. Sun, *J. Am. Chem. Soc.* **2021**, *143*, 15812.

[32] a) L. Huang, Y. Li, Y. Du, Y. Zhang, X. Wang, Y. Ding, X. Yang, F. Meng, J. Tu, L. Luo, C. Sun, *Nat. Commun.* **2019**, *10*, 4871; b) Z. Jiang, B. Yuan, Y. Wang, Z. Wei, S. Sun, O. U. Akakuru, Y. Li, J. Li, A. Wu, *Nano Today* **2020**, *34*, 100910.

[33] M. Bendikov, F. Wudl, D. F. Perepichka, *Chem. Rev.* **2004**, *104*, 4891.

[34] A. Del Prete, P. Zaccagnino, M. Di Paola, M. Saltarella, C. Oliveros Celis, B. Nico, G. Santoro, M. Lorusso, *Free Radic. Biol. Med.* **2008**, *44*, 1443.

[35] F. Weigend, R. Ahlrichs, *Phys. Chem. Chem. Phys.* **2005**, *7*, 3297.

[36] A. Madaan, R. Verma, A. T. Singh, S. K. Jain, M. Jaggi, *J. Biol. Methods* **2014**, *1*, e1.

Table of Contents Graphic

Organic metal adjuvants, assembled from charge-transfer complexes and characterized by broad substrate scope, high accessibility, and flexibly-tuned optical properties, demonstrate strong second near-infrared photoacoustic and photothermal properties as well as high adjuvant abilities by perturbing redox homeostasis to potentiate immunogenicity and immune responsiveness.